Article

Current Biology

Vision and Locomotion Combine to Drive Path Integration Sequences in Mouse Retrosplenial Cortex

Highlights

- Locomotion-gated optic flow drives spatial activity sequences in RSC
- Decoupling vision and locomotion disrupts RSC spatial activity sequences
- Landmark-related visual responses are gated by spatial position
- Spatial activity sequences are anchored to contextual cues

Authors

Dun Mao, Leonardo A. Molina, Vincent Bonin, Bruce L. McNaughton

Correspondence

zjumao@gmail.com (D.M.), vincent.bonin@nerf.be (V.B.), bruce.mcnaughton@uleth.ca (B.L.M.)

In Brief

Mao et al. demonstrate that neurons in the retrosplenial cortex integrate visual inputs, locomotion, and contextual cues to generate spatial activity sequences. This contextual cue-anchored sequential activity could be driven by locomotion-gated optic flow, suggesting a role of the RSC in fusing visual and motor inputs into internal representations.

Mao et al., 2020, Current Biology *30*, 1680–1688
May 4, 2020
https://doi.org/10.1016/j.cub.2020.02.070

CellPress

CellPress

Current Biology
Article

Vision and Locomotion Combine to Drive Path Integration Sequences in Mouse Retrosplenial Cortex

Dun Mao,[1,2,6,8,*] Leonardo A. Molina,[1,7] Vincent Bonin,[2,3,4,*] and Bruce L. McNaughton[1,5,*]
[1]Canadian Centre for Behavioural Neuroscience, Department of Neuroscience, University of Lethbridge, 4401 University Dr W, Lethbridge, AB T1K 3M4, Canada
[2]Neuro-Electronics Research Flanders, Kapeldreef 75, Leuven 3001, Belgium
[3]VIB, Leuven 3000, Belgium
[4]Department of Biology and Leuven Brain Institute, KU Leuven, Naamsestraat 59-Box 2465, Leuven 3000, Belgium
[5]Department of Neurobiology and Behavior, 2205 McGaugh Hall, University of California, Irvine, CA 92697, USA
[6]Present address: Department of Neuroscience, Baylor College of Medicine, 1 Baylor Plaza, Houston, TX 77030, USA
[7]Present address: Hotchkiss Brain Institute, Cumming School of Medicine, University of Calgary, 3330 Hospital Drive NW, Calgary, AB T2N 4N1, Canada
[8]Lead Contact
*Correspondence: zjumao@gmail.com (D.M.), vincent.bonin@nerf.be (V.B.), bruce.mcnaughton@uleth.ca (B.L.M.)
https://doi.org/10.1016/j.cub.2020.02.070

SUMMARY

The retrosplenial cortex (RSC) is involved in a broad range of cognitive functions, integrating rich sensory, motor, and spatial signals from multiple brain areas, including the hippocampal system. RSC neurons show hippocampus-dependent activity reminiscent of place cell sequences. Using cellular calcium imaging in a virtual reality (VR)-based locomotion task, we investigate how the integration of visual and locomotor inputs may give rise to such activity in RSC. A substantial population shows neural sequences that track position in the VR environment. This activity is driven by the conjunction of visual stimuli sequences and active movement, which is suggestive of path integration. The activity is anchored to a reference point and predominantly follows the VR upon manipulations of optic flow against locomotion. Thus, locomotion-gated optic flow, combined with the presence of contextual cues at the start of each trial, is sufficient to drive the sequential activity. A subpopulation shows landmark-related visual responses that are modulated by animal's position in the VR. Thus, rather than fragmenting the spatial representation into equivalent locomotion-based ensemble versus optic-flow-based ensemble, in RSC, optic flow appears to override locomotion signals coherently in the population, when the gain between the two signals is altered.

INTRODUCTION

The retrosplenial cortex (RSC) integrates inputs from multiple sensory and motor cortices, subcortical nuclei, and the hippocampal formation and is involved in various cognitive behaviors, including spatial navigation and multisensory integration [1–4]. Many studies have identified various spatially informative signals in RSC, including head-direction-sensitive signals [5], spatially localized firing [6, 7], and selective responses to cues that are useful for navigation and the location of rewards [8–10]. During free exploration, RSC neurons show periodic spatial activity patterns [11, 12] that encode positions relative to important cues or decision points. Thus, RSC neuronal activity may reflect integration of self-motion signals relative to a reference point. Indeed, behavioral studies have demonstrated that animals with RSC lesions show deficits in path integration in darkness [13, 14].

RSC also participates in visual processing via extensive connections with multiple cortical visual areas, including direct projections from the primary visual cortex [15, 16]. RSC neurons can respond to visual stimuli [17] and encode visual features [18]. Moreover, RSC has been extensively studied as a part of the head-direction system with some neurons exhibiting head-direction tuning that may be referenced to visual landmarks [5, 6, 19, 20]. Therefore, RSC may be important for spatial navigation behaviors involving various visual cues.

Thus, the question arises as to how internal self-motion and external visual inputs influence spatial activity in RSC. Previous experiments with free-moving rodents face challenges in decoupling self-motion cues from visual inputs in a controllable manner. Recent experiments have begun to dissociate the relative contributions of different factors to hippocampal spatial activity by introducing conflict between self-motion and visual inputs [21]. Hippocampal place fields can sometimes rescale dramatically when locomotion and vestibular self-motion cues are eliminated [22]. Under head-restrained conditions, grid cells in the medial entorhinal cortex (MEC) show asymmetric and nonlinear changes when the gain between visual scene and locomotion is manipulated [23], indicating that there is no single source dominating grid cell firing, be it optic flow, locomotion, or visual landmarks.

We have recently shown neuronal activity sequences in RSC that track position and/or task progression during head-fixed treadmill running [7]. Resembling the activity of hippocampal place cells [7], this activity requires intact

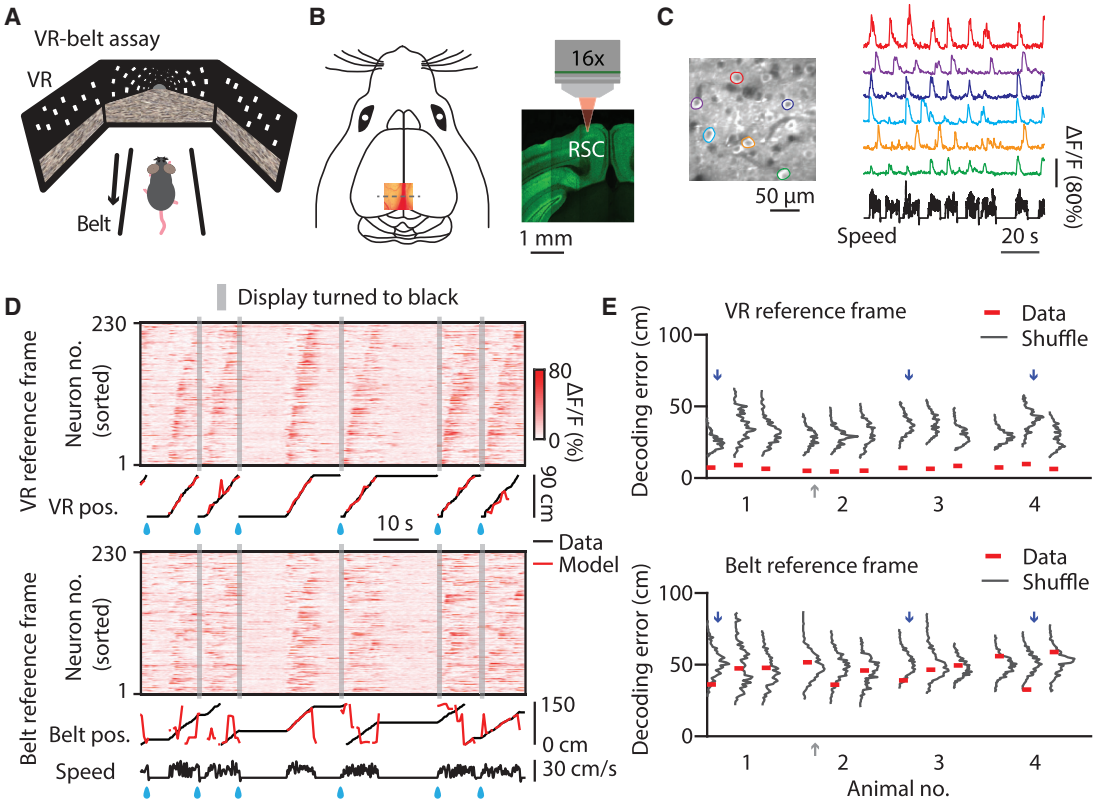

Figure 1. RSC Neural Sequences Encode Virtual Location during Locomotion in the VR Environment

(A) VR-treadmill belt assay with a treadmill apparatus and three displays facing the animal's front, left, and right sides. Movement of the VR scene was triggered by treadmill belt movement. The VR scene was a virtual tunnel of fixed length with pseudo-random visual textures on the wall and floor providing locomotion-related optic flow without strong positional cues.

(B) Left, diagram of a mouse brain with the imaging window above RSC. Sinuses are visible. Right, imaging was performed in transgenic Thy1-GCaMP6s mice targeting superficial agranular RSC. An example histology image (coronal section, at the dashed line in left) is shown.

(C) Example active neurons (left) and corresponding calcium time courses (right, fluorescence signals as a function of time). Speed trace is shown at the bottom.

(D) Top, color-coded calcium time courses for 230 simultaneously imaged neurons ordered by their preferred position in the VR environment—i.e., the position of peak average response. All neurons in the recording were included. Traces below show position in the VR environment, measured (black) and estimated with Bayesian decoding (red). Blue drops indicate time points of reward delivery. Bottom, same calcium time courses ordered by each neuron's preferred position on the treadmill belt. Movement speed is shown at the bottom. The VR track was 90 cm in length and the treadmill track was 150 cm in length. The VR displays were briefly turned to black at the end of each trial (gray bars, 0.5 s).

(E) Decoding errors, absolute value of the difference between measured and estimated position, computed for VR (top) and belt (bottom) position. Data from four animals and three sessions per animal. Horizontal thick red bars indicate mean decoding errors obtained from measured data. Thin gray traces show distributions of decoding errors obtained from shuffled data (1,000 times). Gray arrow indicates the example session shown in (D). Blue arrows indicate the subset of sessions in which belt position decoding errors did not differ significantly from shuffle analysis ($p < 0.05$).

See also Figure S1 and Table S1.

hippocampi and develops with repeated exposure to the same environment [24].

Here, we used cellular functional imaging of RSC neurons and a virtual reality (VR) assay in head-fixed mice. We assessed neural correlates of path integration based on optic flow, locomotion, and contextual cues. We found that locomotion-gated optic flow plays an important role in driving spatial activity sequences that are anchored to contextual cues.

RESULTS

RSC Neural Sequences Track Progress in a Virtual Reality Environment

To study how vision and locomotion drive neuronal activity in RSC, we used a VR-based head-fixed locomotion task (Figure 1A). Transgenic mice (Thy1-GCaMP6s GP4.3, n = 4) [25] were head fixed on a custom VR apparatus and trained to move a 150 cm fabric treadmill for a sucrose water reward while receiving panoramic visual motion stimuli. The mice initiated a trial by moving the treadmill. This triggered display of a VR scene that was updated based on treadmill movement. The visual VR scene was a linear tunnel made of pseudorandom visual textures, which, like the treadmill belt, provided self-motion cues (optic flow) but not salient positional cues. Each trial ended when animals reached the virtual tunnel's end, which corresponded to a fixed travel distance on the treadmill (but not a fixed belt position). The end of the tunnel was signaled by turning the visual display to black and delivering the sucrose water reward followed by a 0.5 s timeout separating the next trial. The distance on the treadmill to traverse the tunnel was set at 90 cm, different

from the length of the treadmill belt. The combination of treadmill locomotion and reward yielded tens of trials in which animals traversed the same VR environment. It also allowed disambiguation of activity linked to reference frames defined by the visual VR and the treadmill belt.

To measure RSC neuronal activity, we used 2-photon calcium imaging through a chronically implanted glass window (Figures 1B, 1C, and S1). Cortical pyramidal neurons in superficial agranular RSC were imaged. We obtained calcium activity time courses of 2,935 neurons (n = 12 sessions, 4 animals) (Table S1). We plotted the calcium time series ordered by locations that elicited their maximal activity (Figure 1D). To identify these locations, we deconvolved calcium time series [26] and calculated the average activity as a function of position in the VR environment or on the treadmill belt. Ordering data by preferred VR location revealed pronounced neural sequences that tracked progress within the VR environment (Figure 1D, top). In contrast, ordering the data by preferred location on the treadmill belt did not show such coordinated activity (Figure 1D, bottom).

To assess encoding of location by RSC neurons, we used Bayesian decoding [24, 27, 28]. From RSC population activity (using all recorded neurons), we calculated estimates of the animal's position in either the VR environment or on the treadmill belt, and compared the accuracy of estimates obtained from measured and randomly shuffled data (2-fold cross validation; STAR Methods). To measure decoding accuracy, we computed decoding errors defined as the mean absolute difference between estimated and observed positions. Decoding of VR position yielded small decoding errors (error = 6.78 ± 1.56 cm; mean ± SD across animals), which differed markedly from shuffle control ($p < 0.001$) (Figure 1E, top; thick red bars versus thin gray traces). In comparison, decoding of belt position yielded large decoding errors (error = 45.58 ± 2.39 cm; mean ± SD across animals), which did not differ significantly from shuffle control ($p > 0.40$ for 8 sessions, $p < 0.10$ for 4 sessions) (Figure 1E, bottom; thick red bars versus thin gray traces). In a subset of the data (three individual sessions from different animals), RSC activity also encoded significant information about belt position ($p < 0.05$) (Figure 1E, blue arrows).

To examine the functional diversity, we identified neurons with selectivity to position in the VR or on the treadmill belt (STAR Methods). Overall, 27% of neurons (801/2,935) showed activity linked to position in the VR environment, 4% of neurons (117/2,935) showed activity correlated with position on the belt, and 3% of neurons (80/2,935) showed activity correlated with both reference frames. The latter group of neurons may have contributed to the good decoding performance in both reference frames for these three sessions (Figure 1E, blue arrows).

To summarize, the above results suggest that during VR-based locomotion, RSC population activity encodes primarily location in the VR reference frame.

Decoupling Visual Inputs and Locomotion Disrupts RSC Neural Sequences

Do RSC neural sequences reflect responses to the visual VR scene or does the activity require conjunction of vision and locomotion? To address this question, we recorded RSC activity in response to synthetic VR trajectories presented independently of the animal's locomotion. This open-loop visual stimulation failed to induce the pronounced sequential activity that was observed during active VR travel (Figures 2A and 2B). It also yielded large decoding errors (error = 16.50 ± 2.43 cm; mean ± SD across animals) (Figure 2D) that did not differ from shuffle control ($p > 0.15$) (Figure 2D; thick red bars versus thin gray traces). This lack of position encoding by RSC population was in striking contrast with the results obtained during closed-loop VR stimulation in matching neuronal populations, which can reliably predict VR position (error = 6.4 ± 0.97 cm, $p < 0.001$; mean ± SD across animals) (Figure 2C, same data as in Figure 1E; one session from each animal). These results show that RSC neural sequences do not reflect mere sensory responses to the VR scene but rather require conjunction of visual and locomotion inputs.

RSC Neural Sequences Reflect Integration of Optic Flow

Do neural sequences observed during VR navigation reflect integration of optic flow from the VR scene, or do they instead reflect distance traveled on the treadmill belt? To distinguish between these possibilities, we studied how RSC population representations of the VR environment are affected by changes in VR gain, which rendered the distance traveled in VR different from distance on the treadmill belt (Figure 3A).

We recorded the activity of the same RSC neuronal populations in consecutive blocks of trials with distinct VR gains (1x, 2x, 0.5x, and 1x) (Table S1), which corresponded to distinct travel distances on the belt (90 cm, 45 cm, 180 cm, and 90 cm). We focused on neurons that encoded information about VR position in the first block (1x) (31%, 570/1,821 neurons; n = 8 sessions, 4 animals) (Table S1) and compared population activity across VR gain conditions. If neuronal activity is driven by optic flow from the VR scene, then the position tuning curves in the VR reference frame would be largely invariant to changes in VR gain. Consistent with this hypothesis, VR position tuning curves were invariant to changes in VR gain (Figure 3A). To quantify potential changes in representations, we computed the Pearson correlation of the population tuning curves as function of VR position across gain conditions. The resulting correlation matrices showed a single, highly significant band along the main diagonal (Figures 3B and 3C; Table S1), confirming invariance of representations across VR gains. The correlation appeared to be higher for the high-gain condition (1x versus 2x) than the low-gain condition (1x versus 0.5x) (Figure 3C; Table S1).

The above results indicate that RSC neural sequences track progress in a VR scene by integrating visual inputs such as optic flow or local features from the textures. To assess whether optic flow alone is sufficient to drive RSC sequential activity, we did additional experiments in which elements of the wall textures of the VR scene were randomly blinked at 10 Hz so that only 10% of texture elements were shown and a unique visual pattern was shown at any given time (Figure 4A). As seen during locomotion in VR scenes with fixed textures, we observed robust sequential activity that could reliably predict the animal's location in the VR environment during travel through this randomly changing environment (Figure 4B). Furthermore, correlation analysis of the measured position tuning curves of the same neuronal population showed strong correlation bands along the main diagonal between different VR gain conditions (Figure 4C). The high-gain condition showed more concentrated bands along the diagonal than the low-gain condition (Figure 4C;

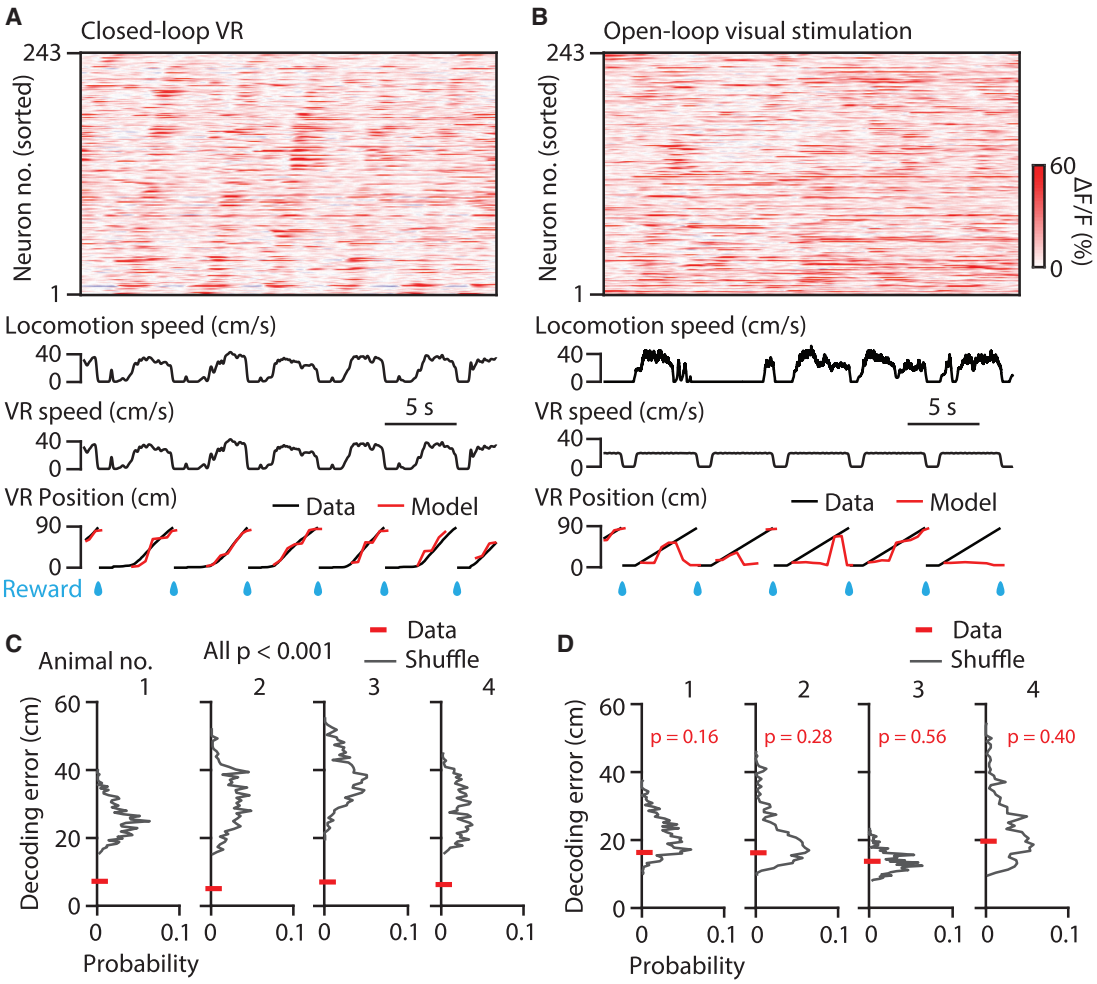

Figure 2. Decoupling Visual Inputs and Locomotion Disrupts RSC Neural Sequences

(A) Top: color-coded, raw calcium time courses for 243 simultaneously imaged neurons during closed-loop VR locomotion; movement in the VR environment was updated based on the animal's locomotion. Calcium time courses were ordered by locations in the VR environment eliciting the largest responses. Locomotion and VR speeds are shown below. Bottom: actual (black) and decoded (red) position traces. Blue drops indicate reward delivery.

(B) The responses of the same neurons as (A) during open-loop VR stimulation (sorted by itself). Open-loop VR scene depicts movement at constant speed through VR environment, regardless of animal's locomotion.

(C) Decoding errors from measured and shuffled data in closed-loop runs (same data as shown Figure 1E). Horizontal thick red bars indicate the decoding errors of the actual data. Thinner gray traces indicate the corresponding distributions of decoding errors for shuffled data (1,000 times). All p values were smaller than 0.001 (actual decoding error relative to the distribution of decoding errors obtainied from shuffled data). n = 4 sessions, 4 animals.

(D) The same as (C) but for the open-loop experiments. Individual p values are indicated.

See also Table S1.

Table S1). Bayesian decoding of VR position from population activity yielded similar accuracy across gains (p = 0.55, 0.49, and 0.72 for decoding window size of 0.3 s, 0.5 s, and 0.7 s, respectively; one-way ANOVA) (Figures 4D and S2).

This confirms that RSC neural sequences are driven by the integration of locomotion-gated optic flow rather than local features, which is suggestive of path integration.

Positional Modulation of Landmark-Related Visual Responses in RSC

To examine how visual landmark encoding is reflected in the activity of RSC neurons, new recordings were made in a distinct VR scene with four identical visual landmarks. The landmarks were presented at four locations (9 cm, 31.5 cm, 54.0 cm, and 76.5 cm) in the VR environment (Figure 5A). Consistent with experiments without landmarks, about 30% of neurons (388/1,312) showed sparse sequential activity involving neurons with significant activation at single VR positions (n = 7 sessions, 3 animals). Some other neurons, rather than the sparse activation, showed repeated activation in lockstep with the visual landmarks (Figures 5B and 5C). Overall, 12% of neurons (152/1,312) showed multiple significant activation points at fixed intervals relative to the visual landmarks (STAR Methods). The neuronal population exhibited repeated sequences activated by the visual landmarks, as shown by the parallel stripes in the correlation matrix (Figure 5D). Within this subpopulation, many neurons (64%,

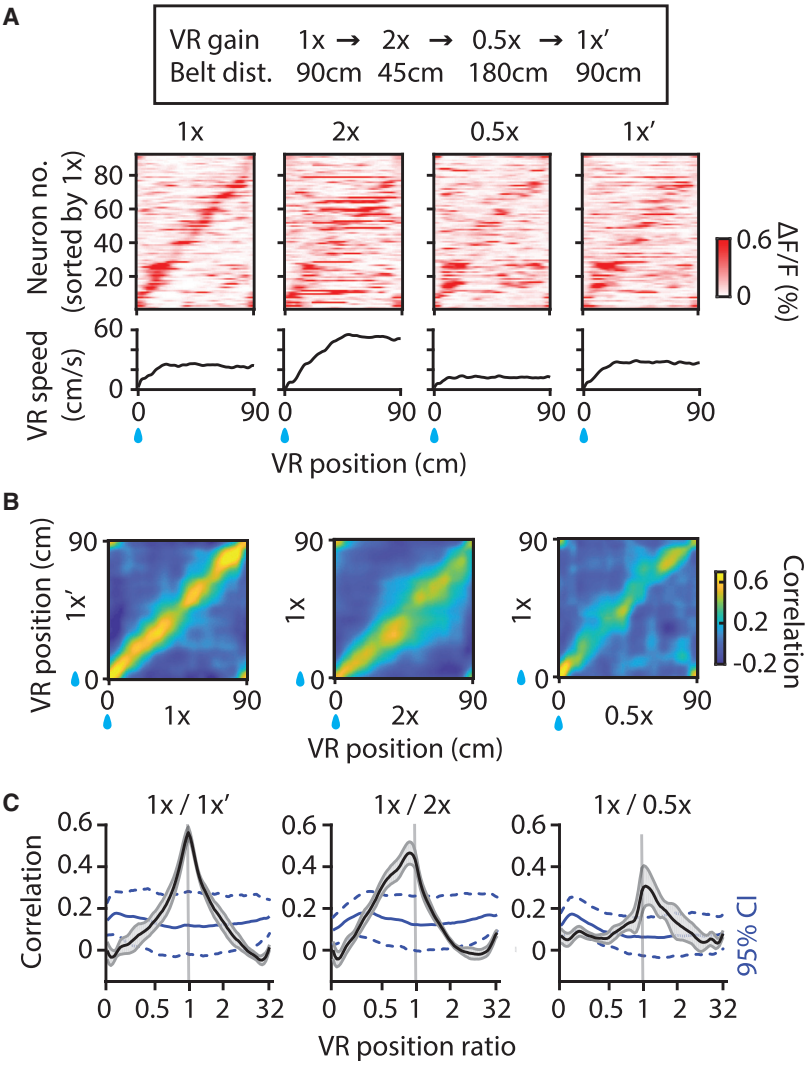

Figure 3. RSC Neural Sequences Track the VR Environment Upon Gain Manipulations

(A) Experiments with different VR gains were performed in consecutive blocks: 1x, 2x, 0.5x, and 1x again. Colormap, sorted neuronal activity of 92 cells (sorted by block 1x) as a function of VR position for an example session. Mean speed traces are shown below.

(B) Mean population vector correlation matrices (across animals, n = 4) between different VR gain conditions.

(C) Mean population vector correlations as a function of VR position ratio. Shaded area, SEM across animals (n = 8 sessions, 4 animals for 1x versus 2x; n = 5 sessions, 4 animals for 1x versus 0.5x and 1x versus 1x′). Solid and dashed blue lines indicate mean and 95% confidence intervals, respectively, of the population vector correlations for shuffled data (1,000 times). Note peak correlations near VR position ratio of 1 (i.e., encoding the same VR position). See also Table S1.

97/152) showed different levels of activation at distinct VR positions, suggesting the modulation of landmark responses by animal's position in VR (Figure 5C; STAR Methods).

Thus, RSC neurons show pronounced, repeatable responses to visual landmarks, which are influenced by animal's position in the VR environment, suggesting an integrated code of internal representation and external stimuli in RSC.

RSC Neural Sequences Are Anchored to Contextual Cues

Finally, we examined how RSC neural sequences are affected by spatial context. We recorded RSC neuronal activity during navigation in a virtual triangle environment made of three connected tunnels that differed only by the visual scene visible at the vertices only after the animals exited the tunnels (Figure 6A; STAR Methods). Randomly blinking dots were presented on the tunnel wall (Figure 6A, bottom), providing optic flow coupled to locomotion. The three vertices were associated with a virtual turn of 120°, reward delivery, and a scene of a classroom environment, which provided a contextual cue indicating the end of the past tunnel and the start of the next tunnel. Some RSC neurons showed multiple activation points at fixed intervals from vertex positions (Figure 6B). About 35% of neurons (342/975) showed significant positional selectivity (STAR Methods) (n = 4 sessions, 2 animals) (Figure 6C). Consistent with a role of path integration, the neuronal populations exhibited repeated activity sequences referenced to the vertex positions (Figures 6C and 6D). A small fraction of these neurons (9.6%, 33/342) showed significantly different firing rates over the three tunnels. The mere presentation of the visual contextual cue and virtual rotation with reward omission was sufficient to reset the neural sequences (Figure S3). Different from the above results, these spatial activity sequences did not reflect responses to the visual landmarks that were not visible from within the tunnels. Instead, the neural sequences may arise from integration of self-motion that was anchored to the reference points at the vertices.

These results indicate that RSC neural sequences can be reset by environmental contextual cues but may be modulated somewhat by the most recent context, even if no longer visible.

DISCUSSION

Our results indicate that vision and locomotion jointly contribute to the generation of spatial activity sequences in RSC. Optic flow plays an important role and, in conjunction with locmotion, is sufficient to drive robust activity sequences. As seen in the hippocampus [21], movement through the environment is necessary. Breaking the coupling between vision and locomotion impairs the spatial activity. The position encoding in the current study likely reflects path integration from a reference point. Similar to what is observed in the primary visual cortex [29], RSC neurons show responses to visual landmarks, and these responses are modulated by animal's spatial position. These responses likely reflect low-level sensory responses, which appear to be gated by internal

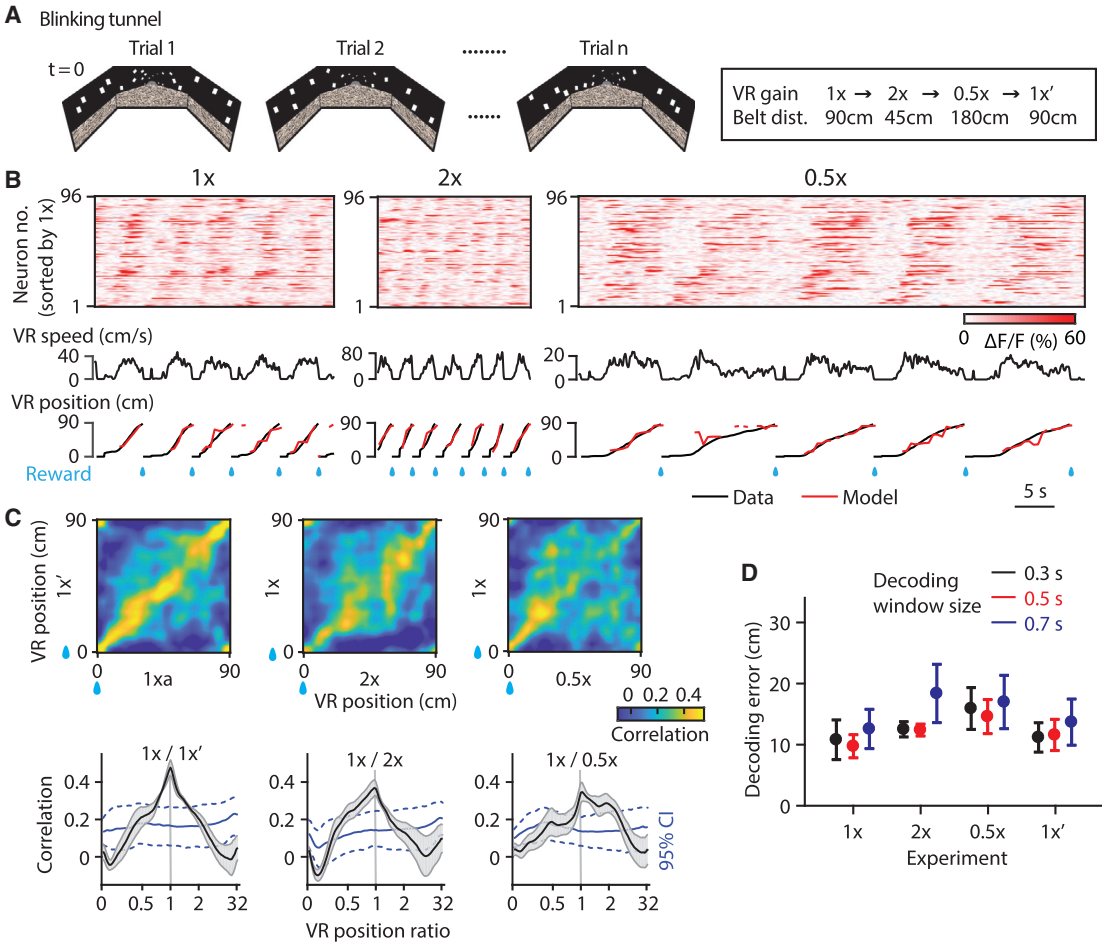

Figure 4. RSC Neural Sequences Integrate Locomotion-Gated Optic Flow

(A) A blinking VR scene with 10% randomly selected squares shown at any given time. The visual scene was unique at any given moment (10 Hz refreshing rate). Experiments with different distinct VR gains were tested in consecutive blocks of trials.

(B) Sorted raw calcium time courses of 96 neurons under different VR gain conditions for an example session. Neurons were sorted by block 1x. Speed and position (actual and decoded) traces are shown below.

(C) Top: population vector correlation matrices between different VR gain conditions. Bottom: mean population vector correlations as a function of VR position ratio. Shaded area, SEM across animals (n = 7 sessions, 4 animals). Solid and dashed blue lines indicate mean and 95% confidence intervals, respectively, of the population vector correlations for shuffled data (1,000 times).

(D) Decoding errors under different VR gain conditions for three different decoding window sizes. Error bars, SEM across animals; n = 4.

See also Figure S2 and Table S1.

path integration signals. Contextual cues can reset RSC neural sequences, with reward being a salient cue. In this way, not only was the entire track coded, but also the segments between any behaviorally significant cues (e.g., left or right turn) [11], or decision points, were encoded in the activity of RSC neurons. Integration of various internal and external cues may generate the periodic activation patterns of RSC neurons that may encode progression between path locations [11, 12]. This is consistent with a broader view of the role of path integration, that it can track multiple vectors based on self-motion information. We speculate that one of the functions of path integration in the current task is to map task progression between salient events.

External sensory cues and internal movement-related information jointly contribute to the spatial code in the hippocampal formation [21–23, 30]. Visual inputs provide information about absolute position from visual landmarks as well as motion signals from optic flow. RSC sits between the visual cortex and the hippocampal formation. The direct influences of visual inputs on spatial coding and path integration may gradually decrease along the RSC-MEC-hippocampus circuit [23]. The hippocampus may globally mediate the generation of neural sequences throughout the cortex [24, 31, 32], which may involve a gain factor determined by internal self-motion information (e.g., locomotion) and externally driven motion cues (e.g., optic flow).

The integrated VR and treadmill assay in head-fixed preparations is a useful tool to dissect the relative contributions of visual and locomotor inputs on the activity in RSC. Other external cues (e.g., tactile, acoustic cues) could also be added

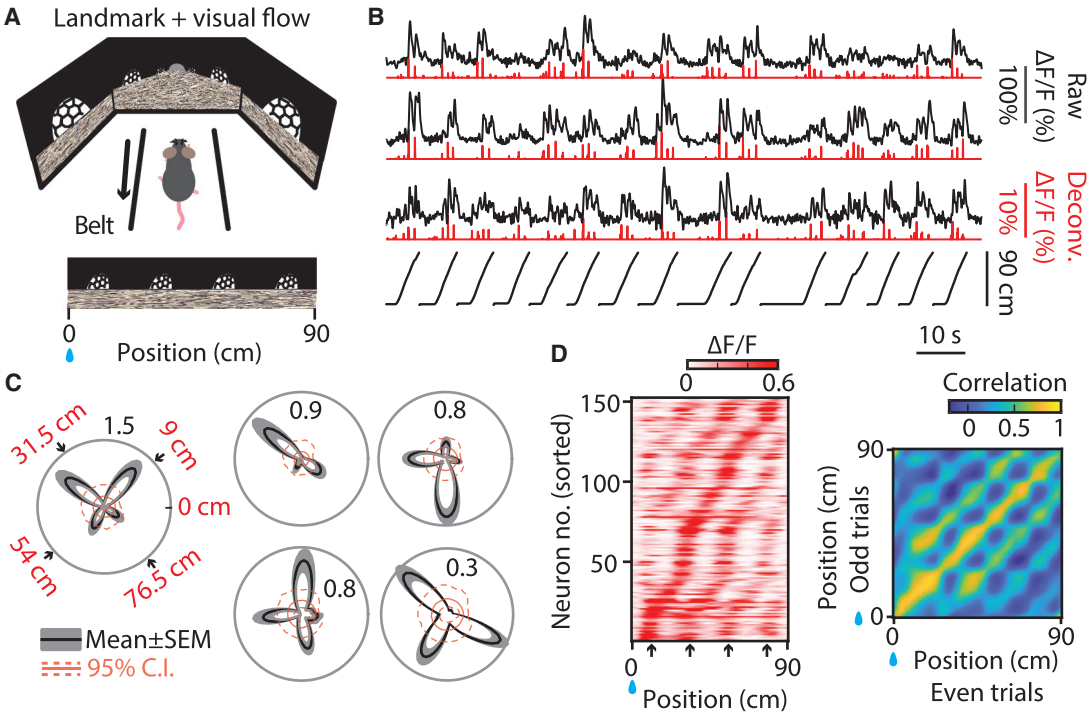

Figure 5. Landmark-Related Visual Responses in RSC Are Modulated by Position

(A) Visual scene with periodic visual landmarks (dome shape, mosaic pattern).

(B) Calcium time courses (raw and deconvolved) for three example neurons showing multiple activation points within a single trial.

(C) Polar plots of the position-mapped responses for five example landmark-responsive neurons. Red color numbers and black arrows indicate landmark positions. Black numbers indicate peak response magnitude (deconvolved ΔF/F). Shaded gray area indicates SEM over trials. Solid and dashed red lines indicate mean and 95% confidence interval, respectively, for the shuffled distributions.

(D) Left: sorted, color-coded neuronal activity for neurons that showed significant landmark-related responses (n = 7 sessions, 3 animals). Right: population vector correlation matrix between even and odd trials for the positional activity map shown on the left. Note relatively high correlation stripes paralleling the main diagonal because of the recurring sequences.

See also Table S1.

to test the influences of other sensory modalities. Head-fixed animals lack acceleration or velocity signals from the vestibular system but not self-motion from limb movement and optic flow. It is possible that the simplified experimental paradigm used here may have masked more complex influences of vision on RSC neuronal responses in a free-movement context. In a free-behavior context, vestibular inputs—including translational and rotational signals and their interactions with vision—may exert strong impacts on the path integration process. The present paradigm may have restrictions similar to those used in human studies using functional magnetic resonance imaging, which investigate the role of optic flow on navigational behavior in a VR setup [33–35]. Previous human studies have shown that the hippocampus and RSC work in concert for successful path integration [34, 36]. The path integration sequences from visual inputs and locomotion in RSC likely result from interactions among multiple regions [37].

Our findings are consistent with the postulated role of RSC in transforming between egocentric and allocentric representations [38], possibly via interactions with the posterior parietal cortex (PPC) [39, 40]. Bottom-up (external) signals from sensory cortices carry environmental information (e.g., derived from optic flow fields) in RSC and PPC, whereas internal, global self-motion representations from the hippocampal formation provide a spatiotemporal substrate to integrate velocity over time to give rise to positional information. As we have shown previously [24], hippocampal outflow is essential for the development of spatial coding in this region of cortex. Information flow is bidirectional, in that RSC back-projects to sensory and motor cortices and forward-projects to the medial temporal lobe (MTL). Within the MTL-RSC-primary cortices framework, sensory/motor cortices could organize behavior based on allocentric information. In addition, MTL could encode or index momentary behavior-relevant (egocentric) sensory experiences [41, 42]. Further work will need to dissect precisely how the top-down and bottom-up signals are integrated in RSC.

STAR★METHODS

Detailed methods are provided in the online version of this paper and include the following:

- KEY RESOURCES TABLE
- LEAD CONTACT AND MATERIALS AVAILABILITY

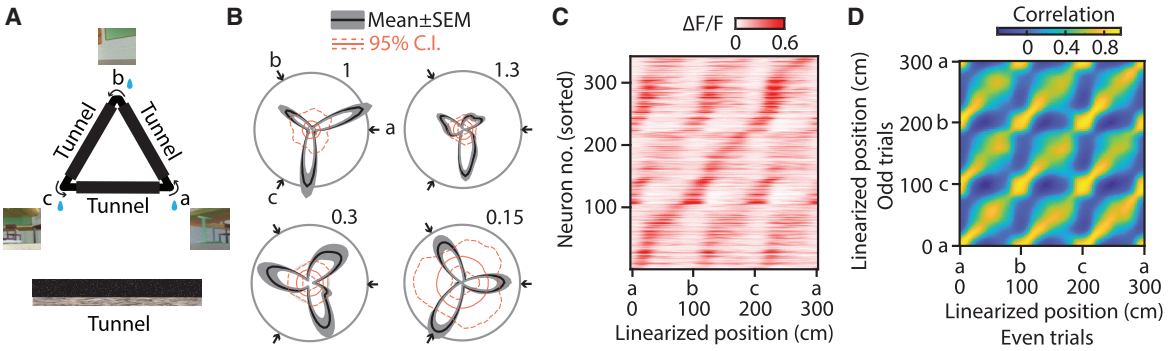

Figure 6. RSC Neural Sequences Are Reset by Contextual Cues

(A) Diagram of the virtual triangle environment. The maze was placed in a big classroom environment. The three vertices were connected by tunnels. Mice ran in the tunnels without seeing the end of the tunnel or the outside environment. Upon exit mice saw the scene of the classroom. A snapshot of the scene is shown. Mice were rewarded and virtually turned by 120° at each vertex. The bottom diagram shows the diagram of the scene within the tunnel. The tunnel wall was decorated with random dots and the floor with pebble patterns.

(B) Polar plots of the position-mapped responses for four example neurons showing multiple activation points. Black arrows indicate vertex positions. Black numbers indicate peak response magnitude (deconvolved ΔF/F). Shaded gray area indicates SEM over trials. Solid and dashed red lines indicate mean and 95% confidence interval of the shuffled distributions.

(C) Sorted, color-coded neuronal activity for neurons that showed significant positional selectivity (n = 4 sessions, 2 animals). Note recurring neural sequences upon vertex positions.

(D) Population vector correlation matrix between even and odd trials for the positional activity map shown in (C). Note relatively high correlation stripes paralleling the main diagonal because of the recurring sequences.

See also Figure S3 and Table S1.

SUPPLEMENTAL INFORMATION

Supplemental Information can be found online at https://doi.org/10.1016/j.cub.2020.02.070.

ACKNOWLEDGMENTS

We thank M. Mohajerani for support, J. Sun and A. Neumann for help with surgeries and experiments, and A. Ayaz for comments. This research was supported through the Alberta Innovates – Health Solutions Polaris award (B.L.M.) and a graduate studentship (D.M.), a Natural Sciences and Engineering Research Council of Canada grant (#RGPIN-2017-03857 to B.L.M.), a National Science Foundation grant (#1631465 to B.L.M.), a Canada Foundation for Innovation grant (#33598 B.L.M.), a Canadian Institutes of Health Research grant (#PJT 156040), a DARPA grant (#HR0011-18-2-0021 to B.L.M.), Research Foundation – Flanders (FWO) grants (G0D0516N and G0C1220N to V.B.), and a KU Leuven Research Council grant (C14/16/048 to V.B.).

AUTHOR CONTRIBUTIONS

D.M., V.B., and B.L.M. designed the study, contributed to the analysis concepts, and wrote the manuscript. L.A.M. devised the virtual reality setup. D.M. performed the experiments and analyzed the data.

DECLARATION OF INTERESTS

The authors declare no competing financial interests.

Received: July 3, 2019
Revised: January 30, 2020
Accepted: February 24, 2020
Published: March 19, 2020

REFERENCES

1. van Groen, T., and Wyss, J.M. (1992). Connections of the retrosplenial dysgranular cortex in the rat. J. Comp. Neurol. *315*, 200–216.
2. Sugar, J., Witter, M.P., van Strien, N.M., and Cappaert, N.L. (2011). The retrosplenial cortex: intrinsic connectivity and connections with the (para)hippocampal region in the rat. An interactive connectome. Front. Neuroinform. *5*, 7.
3. Van Groen, T., and Wyss, J.M. (2003). Connections of the retrosplenial granular b cortex in the rat. J. Comp. Neurol. *463*, 249–263.
4. Sutherland, R.J., Whishaw, I.Q., and Kolb, B. (1988). Contributions of cingulate cortex to two forms of spatial learning and memory. J. Neurosci. *8*, 1863–1872.
5. Chen, L.L., Lin, L.H., Green, E.J., Barnes, C.A., and McNaughton, B.L. (1994). Head-direction cells in the rat posterior cortex. I. Anatomical distribution and behavioral modulation. Exp. Brain Res. *101*, 8–23.
6. Cho, J., and Sharp, P.E. (2001). Head direction, place, and movement correlates for cells in the rat retrosplenial cortex. Behav. Neurosci. *115*, 3–25.
7. Mao, D., Kandler, S., McNaughton, B.L., and Bonin, V. (2017). Sparse orthogonal population representation of spatial context in the retrosplenial cortex. Nat. Commun. *8*, 243.

8. Smith, D.M., Barredo, J., and Mizumori, S.J. (2012). Complimentary roles of the hippocampus and retrosplenial cortex in behavioral context discrimination. Hippocampus *22*, 1121–1133.
9. Vedder, L.C., Miller, A.M.P., Harrison, M.B., and Smith, D.M. (2017). Retrosplenial Cortical Neurons Encode Navigational Cues, Trajectories and Reward Locations During Goal Directed Navigation. Cereb. Cortex *27*, 3713–3723.
10. Chinzorig, C., Nishimaru, H., Matsumoto, J., Takamura, Y., Berthoz, A., Ono, T., and Nishijo, H. (2019). Rat Retrosplenial Cortical Involvement in Wayfinding Using Visual and Locomotor Cues. Cereb. Cortex, bhz183.
11. Alexander, A.S., and Nitz, D.A. (2015). Retrosplenial cortex maps the conjunction of internal and external spaces. Nat. Neurosci. *18*, 1143–1151.
12. Alexander, A.S., and Nitz, D.A. (2017). Spatially Periodic Activation Patterns of Retrosplenial Cortex Encode Route Sub-spaces and Distance Traveled. Curr Biol. *27*, 1551–1560.
13. Cooper, B.G., and Mizumori, S.J. (1999). Retrosplenial cortex inactivation selectively impairs navigation in darkness. Neuroreport *10*, 625–630.
14. Cooper, B.G., Manka, T.F., and Mizumori, S.J. (2001). Finding your way in the dark: the retrosplenial cortex contributes to spatial memory and navigation without visual cues. Behav. Neurosci. *115*, 1012–1028.
15. Wang, Q., Sporns, O., and Burkhalter, A. (2012). Network analysis of corticocortical connections reveals ventral and dorsal processing streams in mouse visual cortex. J. Neurosci. *32*, 4386–4399.
16. Wang, Q., and Burkhalter, A. (2007). Area map of mouse visual cortex. J. Comp. Neurol. *502*, 339–357.
17. Murakami, T., Yoshida, T., Matsui, T., and Ohki, K. (2015). Wide-field Ca(2+) imaging reveals visually evoked activity in the retrosplenial area. Front. Mol. Neurosci. *8*, 20.
18. Powell, A., Connelly, W.M., Vasalauskaite, A., Nelson, A., Vann, S.D., Aggleton, J.P., Sengpiel, F., and Ranson, A. (2019). Stable encoding of visual cues in the mouse retrosplenial cortex. bioRxiv. https://doi.org/10.1101/785139.
19. Chen, L.L., Lin, L.H., Barnes, C.A., and McNaughton, B.L. (1994). Head-direction cells in the rat posterior cortex. II. Contributions of visual and ideothetic information to the directional firing. Exp. Brain Res. *101*, 24–34.
20. Jacob, P.Y., Casali, G., Spieser, L., Page, H., Overington, D., and Jeffery, K. (2017). An independent, landmark-dominated head-direction signal in dysgranular retrosplenial cortex. Nat. Neurosci. *20*, 173–175.
21. Chen, G., King, J.A., Burgess, N., and O'Keefe, J. (2013). How vision and movement combine in the hippocampal place code. Proc. Natl. Acad. Sci. USA *110*, 378–383.
22. Terrazas, A., Krause, M., Lipa, P., Gothard, K.M., Barnes, C.A., and McNaughton, B.L. (2005). Self-motion and the hippocampal spatial metric. J. Neurosci. *25*, 8085–8096.
23. Campbell, M.G., Ocko, S.A., Mallory, C.S., Low, I.I.C., Ganguli, S., and Giocomo, L.M. (2018). Principles governing the integration of landmark and self-motion cues in entorhinal cortical codes for navigation. Nat. Neurosci. *21*, 1096–1106.
24. Mao, D., Neumann, A.R., Sun, J., Bonin, V., Mohajerani, M.H., and McNaughton, B.L. (2018). Hippocampus-dependent emergence of spatial sequence coding in retrosplenial cortex. Proc. Natl. Acad. Sci. USA *115*, 8015–8018.
25. Dana, H., Chen, T.-W., Hu, A., Shields, B.C., Guo, C., Looger, L.L., Kim, D.S., and Svoboda, K. (2014). Thy1-GCaMP6 transgenic mice for neuronal population imaging in vivo. PLoS ONE *9*, e108697.
26. Pnevmatikakis, E.A., Soudry, D., Gao, Y., Machado, T.A., Merel, J., Pfau, D., Reardon, T., Mu, Y., Lacefield, C., Yang, W., et al. (2016). Simultaneous Denoising, Deconvolution, and Demixing of Calcium Imaging Data. Neuron *89*, 285–299.
27. Davidson, T.J., Kloosterman, F., and Wilson, M.A. (2009). Hippocampal replay of extended experience. Neuron *63*, 497–507.
28. Zhang, K., Ginzburg, I., McNaughton, B.L., and Sejnowski, T.J. (1998). Interpreting neuronal population activity by reconstruction: unified framework with application to hippocampal place cells. J. Neurophysiol. *79*, 1017–1044.
29. Saleem, A.B., Diamanti, E.M., Fournier, J., Harris, K.D., and Carandini, M. (2018). Coherent encoding of subjective spatial position in visual cortex and hippocampus. Nature *562*, 124–127.
30. Gothard, K.M., Skaggs, W.E., and McNaughton, B.L. (1996). Dynamics of mismatch correction in the hippocampal ensemble code for space: interaction between path integration and environmental cues. J. Neurosci. *16*, 8027–8040.
31. Whishaw, I.Q., Hines, D.J., and Wallace, D.G. (2001). Dead reckoning (path integration) requires the hippocampal formation: evidence from spontaneous exploration and spatial learning tasks in light (allothetic) and dark (idiothetic) tests. Behav. Brain Res. *127*, 49–69.
32. Fournier, J., Saleem, A.B., Diamanti, E.M., Wells, M.J., Harris, K.D., and Carandini, M. (2019). Modulation of visual cortex by hippocampal signals. bioRxiv. https://doi.org/10.1101/586917.
33. Zajac, L., Burte, H., Taylor, H.A., and Killiany, R. (2019). Self-reported navigation ability is associated with optic flow-sensitive regions' functional connectivity patterns during visual path integration. Brain Behav. *9*, e01236.
34. Sherrill, K.R., Erdem, U.M., Ross, R.S., Brown, T.I., Hasselmo, M.E., and Stern, C.E. (2013). Hippocampus and retrosplenial cortex combine path integration signals for successful navigation. J. Neurosci. *33*, 19304–19313.
35. Taube, J.S., Valerio, S., and Yoder, R.M. (2013). Is navigation in virtual reality with FMRI really navigation? J. Cogn. Neurosci. *25*, 1008–1019.
36. Chrastil, E.R., Sherrill, K.R., Hasselmo, M.E., and Stern, C.E. (2015). There and Back Again: Hippocampus and Retrosplenial Cortex Track Homing Distance during Human Path Integration. J. Neurosci. *35*, 15442–15452.
37. Wolbers, T., Wiener, J.M., Mallot, H.A., and Büchel, C. (2007). Differential recruitment of the hippocampus, medial prefrontal cortex, and the human motion complex during path integration in humans. J. Neurosci. *27*, 9408–9416.
38. Byrne, P., Becker, S., and Burgess, N. (2007). Remembering the past and imagining the future: a neural model of spatial memory and imagery. Psychol. Rev. *114*, 340–375.
39. Wilber, A.A., Clark, B.J., Forster, T.C., Tatsuno, M., and McNaughton, B.L. (2014). Interaction of egocentric and world-centered reference frames in the rat posterior parietal cortex. J. Neurosci. *34*, 5431–5446.
40. Clark, B.J., Simmons, C.M., Berkowitz, L.E., and Wilber, A.A. (2018). The retrosplenial-parietal network and reference frame coordination for spatial navigation. Behav. Neurosci. *132*, 416–429.
41. Teyler, T.J., and DiScenna, P. (1986). The hippocampal memory indexing theory. Behav. Neurosci. *100*, 147–154.
42. McNaughton, B.L. (2010). Cortical hierarchies, sleep, and the extraction of knowledge from memory. Artif. Intell. *174*, 205–214.
43. Pachitariu, M., Stringer, C., Schröder, S., Dipoppa, M., Rossi, L.F., Carandini, M., and Harris, K.D. (2016). Suite2p: beyond 10,000 neurons with standard two-photon microscopy. bioRxiv. https://doi.org/10.1101/061507.
44. Goldey, G.J., Roumis, D.K., Glickfeld, L.L., Kerlin, A.M., Reid, R.C., Bonin, V., Schafer, D.P., and Andermann, M.L. (2014). Removable cranial windows for long-term imaging in awake mice. Nat. Protoc. *9*, 2515–2538.
45. Kirkcaldie, M. (2012). Neocortex. In The Mouse Nervous System, C. Watson, G. Paxinos, and L. Puelles, eds. (Elsevier), pp. 52–111.
46. Bonin, V., Histed, M.H., Yurgenson, S., and Reid, R.C. (2011). Local diversity and fine-scale organization of receptive fields in mouse visual cortex. J. Neurosci. *31*, 18506–18521.
47. Chen, T.W., Wardill, T.J., Sun, Y., Pulver, S.R., Renninger, S.L., Baohan, A., Schreiter, E.R., Kerr, R.A., Orger, M.B., Jayaraman, V., et al. (2013). Ultrasensitive fluorescent proteins for imaging neuronal activity. Nature *499*, 295–300.
48. Skaggs, W.E., McNaughton, B.L., Gothard, K.M., and Markus, E.J. (1993). An information-theoretic approach to deciphering the hippocampal code. In Advances in Neural Information Processing Systems (Citeseer), pp. 1030–1037.

STAR★METHODS

KEY RESOURCES TABLE

REAGENT or RESOURCE	SOURCE	IDENTIFIER
Deposited Data and Code		
Preprocessed data and code	https://gin.g-node.org/dunmao/RSC_OpticFlow	N/A
Chemicals, Peptides, and Recombinant Proteins		
C & B Metabond	Parkell	Cat# S380
Vetbond	3M	Cat# 1469SB
Optical glue	Norland	Cat# NOA71
Experimental Models: Organisms/Strains		
Mouse: C57BL/6J-Tg(Thy1-GCaMP6s)GP4.3Dkim/J	The Jackson Laboratory	RRID: IMSR_JAX:024275
Software and Algorithms		
Blender 2.79	Blender Foundation	RRID: SCR_008606
MATLAB (R2017a)	MathWorks	RRID: SCR_001622
Suite 2P	[43]	N/A
Deconvolution algorithm	[26]	N/A
Other		
Tablets	Samsung	SM-T230N
Microcontroller	Adruino	Mega 2560
Treadmill	Custom built	N/A
Treadmill belt	Country Brook	L-BLA-2
Data acquisition	Axon Instruments	Digidata 1322A
2-photon microscope	Thorlabs	Bergamo II
Head plate	Custom made	N/A

LEAD CONTACT AND MATERIALS AVAILABILITY

Further information and requests should be directed to and will be fulfilled by the Lead Contact, Dun Mao (zjumao@gmail.com). This study did not generate new unique reagents.

EXPERIMENTAL MODEL AND SUBJECT DETAILS

Animals

All animal procedures were performed in compliance with the protocols approved by the ethical research committee of the University of Lethbridge. Four Thy1-GCaMP6s GP4.3 [25] (RRID: IMSR_JAX:024275) male mice (20-25 g, 2-4 months old at the time of surgery) were used in this study. This transgenic mouse line was selected for its strong and stable expression of GCaMP6s in a large fraction of cortical excitatory neurons. Mice were group-housed before surgeries and individually housed afterward. After head-plate implantation, mice were habituated to head fixation over a few days and trained to move on a treadmill. Mice were maintained under 12-h light/dark cycle throughout, kept on water restriction and their body weights were maintained around 85% of their baseline weights. After all experiments, mice were perfused to allow for brain histology.

METHOD DETAILS

Surgical procedures

Mice were implanted with a head-plate and a removable cranial window [44]. Briefly, mice were injected with dexamethasone (0.2 mg/kg, intramuscular) 2 h before surgery, and anesthetized with isoflurane (1%–1.5%, O_2: 0.5-1 L/min) with body temperature maintained at 37°C. A custom-made head-plate was attached to the skull using adhesive cement (C&B-metabond, Parkell) and acrylic material (TAB 2000, Kerr). Two rubber rings were attached to the head-plate using superglue. Then mice were allowed to recover for one week and behavior training started. After 2-3 weeks of training, a 2nd phase surgery was performed. Mice were prepared in the same way as during the 1st phase surgery. A 3 mm diameter craniotomy was made with a dental drill (600 μm tip) over the

retrosplenial cortex across the midline, centered at ~2 mm from lambda [45]. The craniotomy was rinsed and covered with artificial cerebrospinal fluid (ACSF). A cranial window made of 3 circular (one 5 mm, two 3 mm) coverslips (affixed with optical adhesive NOA71, Norland) was implanted and attached to the skull using Vetbond tissue adhesive (3M) and acrylic material [44].

Behavioral training

After recovery from the 1st phase surgery, mice were trained to be head-fixed and to move on a training treadmill. The treadmill belt length was 120 cm. The belt was made from Velcro material and free of texture patches on its surface. The movement of the belt was guided by 2 3-D printed wheels. A rotation encoder was used to monitor belt movement. A pinch valve was used for reward delivery through a microcontroller (Arduino Mega 2560). Mechanical parts were obtained from Thorlabs. Mice were under water restriction for the course of the training and imaging experiments. Mice were trained to actively move the treadmill belt to obtain a drop of sucrose water reward at the end of each trial. Their body weights were monitored and maintained at around 85% of normal weights. After 2-3 weeks of training, the 2nd phase surgery was performed and mice were allowed to recover for another week. Then mice were re-habituated to the training treadmill for 1 week and imaging experiments started on a separate experiment treadmill integrated with a VR setup, which was at a distinct location in the room. The experiment treadmill and VR was placed under the 2-photon microscope. The treadmill belt length was 150 cm. Therefore, the experiment treadmill and VR setup were novel to the mice on the first day imaging data were collected.

Integrated VR and treadmill belt assay

Three Android-based (Android 4.2) tablets (Samsung SM-T230N) (one in the front, one on the left and the third on the right, covering a total of ~240° visual field) displaying visual scene synchronized to treadmill motion were used to construct the VR. The VR environment was created using Blender 2.79 (Blender Foundation). The rendering program was developed and compiled using Unity (Unity Technologies). All behavioral data were recorded in a data acquisition system (Axon Digidata 1322A), which was also used to trigger and synchronize with imaging data. The distance to run for each trial in the VR was always 90 cm. At the end of each trial, VR was instantaneously turned off for 0.5 s and reward was delivered and next trial started. In the random square experiment (Figures 1–3), the visual scene was composed of white squares randomized on the wall and pebbles on the floor. The same scene was played across trials. Under normal condition (1x), VR was calibrated such that the distance run in the VR matched to the distance run on the belt (i.e., locomotion distance). In the blinking square experiment, at any given time, only 10% randomly selected white squares were shown (Figure 4). The visual scene was refreshed every 0.1 s. In the visual landmark experiment, the random square visual pattern on the wall was replaced by half-dome white mosaic, which was presented at 4 equidistant positions along the VR track: 9, 31.5, 54.0, and 76.5 cm (Figure 5). Each mosaic pattern covered about 10 cm VR distance. Each mosaic pattern moved from central to lateral 120° visual field as the mice moved through the track. The same pebble scene was used on the floor. Thus, both optic flow and landmarks were available.

In the virtual triangle maze experiment, the maze was placed in a classroom environment. The maze was consisted of three tunnels that were connected at the three vertices. Mice ran within the tunnels by moving on the treadmill belt. The tunnels had random dots on the wall and pebble patterns on the floor. Mice did not see the external environment or the end while running in the tunnels. Upon exit, mice saw the classroom environment, were virtually rotated by 120° (by turning the classroom environment in VR), and a drop of sucrose water was delivered. Then mice entered the next tunnel. Mice traversed the three tunnels that were interleaved by different contextual cues unidirectionally. In the reward omission experiment, the reward at the north vertex (vertex b) was omitted.

VR gain manipulation experiments

Under 1x VR gain condition, VR moved at the same speed as locomotion speed. Under 2x VR gain condition, VR moved at twice the speed of the locomotion speed. Under 0.5x VR gain condition, VR moved at half the speed of the locomotion speed. Across different VR gain conditions, the distance for each trial in the VR was always 90 cm. The corresponding distance for each trial on the treadmill belt was 90 cm, 45 cm, and 180 cm, for 1x, 2x, and 0.5x VR gain, respectively. Experiments with different VR gains were ran in blocks, i.e., 1x, 2x, 0.5x, and 1x again, with each block lasting 5-10 min. In the open-loop experiments, the visual scene was decoupled from animal's locomotion and played at constant speed 18 cm/s. Mice were rewarded with a drop of sucrose water at the end of each trial and next trial started.

Two-photon imaging

Population of RSC neurons at 100-200 μm from dorsal surface (for superficial agranular RSC) were imaged using a Bergamo II multiphoton microscope (Thorlabs). A Ti:Sapphire excitation laser (Coherent) was operated at 920 nm (~20-120 mW laser power at the sample) through a 16x lens (NA = 0.8, Nikon). Green fluorescence from GCaMP6s was collected and measured with a GaAsP photomultiplier tubes (PMTs). Blackout fabric was used to prevent stray light from entering the objective and PMTs. Images were collected at ~20 frames per second. Imaging window was centered at around 2.5 mm from the traverse sinus and 0.5 mm from the midline sinus. The field of view was 835 × 835 μm in size.

QUANTIFICATION AND STATISTICAL ANALYSIS

Image pre-processing and quantification of calcium activity

Data analysis was performed using MATLAB (R2017a, The Mathworks). Somatic calcium activity time courses were extracted using Sutie2P [43]. Images were registered to correct for translational XY motion. Regions of interest (ROIs) over neuronal cell bodies were identified by using local pixel correlation analysis. All ROIs were then visually inspected and putative non-somatic ROIs were manually excluded. The baseline-subtracted ΔF/F0 was calculated for each ROI using the summed value of all pixels corresponding to that ROI [46] by subtracting the summed value of a single layer of pixels that surrounded the cell body [47]. The raw time-courses were deconvolved for further analysis using constrained nonnegative matrix factorization [26].

Statistics

Exact p values were reported except for p values smaller than 0.001 which were reported as $p < 0.001$. Unless stated otherwise, statistical significance for all data analyses was assessed by comparing the results from original data to the results obtained from 1000 random permutations obtained by randomly and circularly shifting calcium activity time courses relative to the recorded behavioral data. If the actual data were beyond the 95% confidence interval of the resampled distribution, it was considered as significant. Data were written in mean ± SEM over animals (otherwise indicated). Detailed quantifications for each figure were listed in Table S1.

Detection of neurons with spatial activity

Data shown in Figures 1 and 2 were based on all imaged, active neurons. Data shown in Figures 3–6 were based on neurons showing significant spatial activity. We used two methods to select neurons that showed spatial activity. Deconvolved data were used. In the first method, the entire linear track was divided into 100 position bins and occupancy-normalized activity was smoothed using a Gaussian window (SD = 3 position bins) for each neuron. Trial-averaged activity as well as the standard error across trials as a function of position was obtained. We then circularly shifted the neuronal activity trace in time for a random time between 20 and session duration less 20 s, and obtained the trial-averaged, occupancy-normalized activity as a function of position. We repeated this process for 1000 times and obtained the mean and 95% confidence interval of the shuffled distribution. If the lower bound of the actual activity (mean-SEM) in any position bin across trials was greater than the 97.5 percentile of the shuffled distribution, then the neuron was considered to carry significant spatial activity. In the landmark experiment (Figure 5), if the neuron had more than one local maxima that was significantly greater than the shuffled distribution (i.e., lower bound larger than 97.5 percentile), and the local maxima was at fixed position from its preceding landmarks (difference < 5 cm, for at least 2 landmarks), it was considered as encoding position from landmarks, i.e., landmark vector cells. Within the landmark vector cells, we compared the activity as a function of position across trials and identified neurons that showed significantly different responses to the 4 landmarks using one-way ANOVA.

In the second method, neurons with place cell characteristics were identified based on spatial information content. Original spatial information was calculated using the following formula [48]:

$$SI = \sum_{i=1}^{N} p_i \frac{f_i}{f} \log_2 \frac{f_i}{f}$$

where p_i is the occupancy probability (the fraction of time spent) in the i-th position bin; f_i is the occupancy-normalized activity (summed activity divided by the total time spent) in the i-th position bin; f is the overall activity (summed f_i over all bins); and N is the number of position bins (N = 100). Resampled spatial information distribution was obtained by circularly shifting the neuronal activity relative to the position trace by a random time between 20 and session duration less 20 s for 1000 times. If the original spatial information is greater than 97.5 percentile of the shuffled distribution, it was considered as carrying significant spatial information.

These two methods in selecting spatially responsive cells yielded qualitatively similar results. Results shown in the paper were based on the first method.

The position that elicited the largest response in the trial-averaged, occupancy-normalized position tuning curves was used to sort neurons across all figures.

Bayesian decoding of position from calcium activity time courses

All neurons imaged in a single session were used for position decoding. We adapted a Bayesian approach to build a probability distribution of position given the population activity (i.e., population vector) at each time bin (non-overlapping 0.5 s window) [24, 27]. The size of the time window was selected to minimize the decoding error [24]. Position decoding was performed for period where the movement speed was above 1 cm/s. Training and testing trials were separated (odd trials for training and even trials for testing). Decoding error was defined as the median error of the entire session. Resampled decoding error distributions were obtained by circularly shifting the time courses of all neurons relative to the position trace by a random time between 20 and session duration less 20 s for 1000 times. The population activity was considered to significantly code position if the actual decoding error is lower than

5 percentile of the shuffled distribution. The detailed decoding algorithm is described below, we aimed to estimate the probability of animal's position given all neurons' activity in a short time window:

$$P\left(pos\left|\left(\frac{dF}{F}\right)_{all}\right.\right) = \frac{P\left((dF/F)_{all}\left|pos\right.\right) \times P(pos)}{P\left((dF/F)_{all}\right)}$$

where *pos* denotes position; $(dF/F)_{all}$ is the activity of all imaged neurons (population vector); *P* stands for probability. $P(pos)$ is the fraction of time the animal spent in each position bin. Given the assumption of independent firing and Poisson distribution of firing rates, we have:

$$P\left(\left(\frac{dF}{F}\right)_{all}\middle|pos\right) = \prod_{i=1}^{N} P\left(\left(\frac{dF}{F}\right)_{i}\middle|pos\right) = \prod_{i=1}^{N} \frac{(\tau f_i(pos))^{n_i}}{n_i!} e^{-\tau f_i(pos)}$$

where τ is the size of the time bin (0.5 s); $f_i(pos)$ is the position tuning curve (trial-averaged and occupancy-normalized) for the *i*-th neurons (using only odd trials); *N* is the total number of neurons; n_i is the mean activity of the *i*-th neuron within that time bin. Thus, we have,

$$P\left(pos\left|\left(\frac{dF}{F}\right)_{all}\right.\right) = C\left(\prod_{i=1}^{N} f_i(pos)^{n_i}\right) e^{-\tau \sum_{i=1}^{N} f_i(pos)}$$

where C is a normalization factor such that $P(pos|(dF/F)_{all})$ sums to 1. $P(pos|(dF/F)_{all})$ is the probability distribution of position for the current time bin. Position with the maximum probability was considered as the decoded position for the current time bin.

Population vector correlation analysis

Trial-averaged, occupancy-normalized position activity for all identified spatially responsive cells (population vector) at each position bin (100 bins) under one condition (e.g., 1x VR gain) was correlated (Pearson linear correlation) with that under another condition (e.g., 2x VR gain) to obtain the population vector correlation matrix. The mean population vector correlation as a function of position ratio in the VR or belt reference frame was obtained by the projection of the correlation matrix along paths radiating from the origin. Correlation along the path was averaged. The tangent of the angle of corresponding path corresponded to the VR position ratio between conditions. There was one-to-one correspondence between VR position and belt distance ratios. A significant maxima in the resulting correlation curve at the VR position ratio of 1 indicated that the population tracks position in the VR. A significant maxima at the belt distance ratio of 1 indicated the population activity reflect locomotion-based path integration. The 95% confidence interval of the resampled correlation distribution was obtained by circularly shifting the neuronal time courses relative to the position trace by a random time between 20 and session duration less 20 s for 1000 times. For each shuffling, the resulting average population vector was then correlated with that of the block it was compared to. The 95% CI of the correlation at each position/distance ratio was the 2.5 and 97.5 percentiles of the resampled correlation distribution.

DATA AND CODE AVAILABILITY

The preprocessed data and essential code are deposited at (https://gin.g-node.org/dunmao/RSC_OpticFlow). Further requests should be directed to any of the corresponding authors.